

# Effect of *tert*-Butylation on the Photophysics of Thermally Activated Delayed Fluorescence Emitters

Kalyani Thakur, Bas van der Zee, Oskar Sachnik, Constantin Haese, Robert Graf, Jasper J. Michels, Gert-Jan A. H. Wetzelaer, Charusheela Ramanan, and Paul W. M. Blom\*

Thermally activated delayed fluorescence (TADF) emitters potentially can provide organic light-emitting diodes with 100% internal quantum efficiency by harvesting triplet excitons. Generally, TADF emitters are small molecules that are not applicable for solution processability. The addition of *tert*-butyl groups to the periphery of TADF emitters has proven to improve their solubility in various organic solvents, reduce aggregation-induced quenching, and enhance the photoluminescence quantum yield (PLQY). This article studies the photophysical influence of the *tert*-butyl group attached to an emitter with a carbazole acceptor and a triazine donor. The resulting t3CzTrz-F is a blue–green TADF emitter, in which the addition of a *tert*-butyl group increases the rate of reverse intersystem crossing (rISC), while simultaneously decreasing the nonradiative decay rate substantially. In addition, dilution of t3CzTrz-F in a host matrix in film results in an enhanced PLQY, which is associated with a decrease in the nonradiative decay constant, while there is no change in the rISC rate. Through a solid-state NMR study, the change in rISC and nonradiative rate upon *tert*-butylation by enlarged intermolecular spacing and reduced vibrational and rotational freedom is rationalized, resulting in improved photophysical performance.

## 1. Introduction


Thermally activated delayed fluorescence (TADF) emitters are a promising third generation of organic light-emitting diode (OLED) materials, which have the capability of harvesting triplet excitons in order to obtain 100% internal quantum efficiency (IQE).<sup>[1,2]</sup> In such emitters, electron-donor and -acceptor moieties are coupled into configurations which yield small singlet–triplet splitting, thus promoting reverse intersystem crossing

(rISC) of the initially nonradiative triplet state to the radiative singlet state. Highly efficient TADF OLEDs have been demonstrated, typically with small-molecule emitters embedded in a multilayer structure,<sup>[3]</sup> reaching IQEs close to  $\approx 100\%$ .<sup>[4]</sup> In such vacuum-deposited devices, external quantum efficiencies (EQEs) exceeding 30% have been reported.<sup>[5]</sup> However, especially for blue TADF emitters there are still some major challenges to overcome. One issue is the efficiency roll-off, which is the reduced efficiency at higher brightness, at which most commercial applications operate.<sup>[6]</sup> Another problem is that the operational lifetime of TADF OLEDs is still impractically low for commercial purposes,<sup>[6,7]</sup> something that is exacerbated by the inherently high exciton energies of blue emitters. Therefore, a lot of research nowadays focusses on achieving stable TADF emitters with blue emission.

There is also a drive to develop solution-processable TADF materials, which are highly desirable from a commercialization standpoint. The fabrication costs associated with the more standard thermal evaporation method, which requires high vacuum and good thermal stability of the material,<sup>[8]</sup> are relatively high, making it less suited for large-area fabrication.<sup>[9]</sup> On the other hand, solution-processable methods such as spin coating, spray coating, and inkjet printing are more desirable for large-scale and low-cost fabrication.<sup>[10]</sup> A large number of materials including small molecule, dendrimer, and polymer materials have been synthesized with the goal to simultaneously achieve excellent TADF characteristics, having the right color coordinate in the blue region, and to be solution processable.<sup>[5,11]</sup> Furthermore, OLED devices fabricated using solution-processable TADF materials are compatible with flexible substrates and generate a relatively small amount of waste,<sup>[5]</sup> making a purely organic solution-processable TADF OLED with high efficiency the aim, but this remains a challenge.

The main condition to achieve solution processing requires good miscibility of the material in organic solvents and ability to form a homogenous film.<sup>[11]</sup> For small molecules, a common approach to achieve solution processability is to dope them in a wide bandgap host.<sup>[12–14]</sup> This leads to a myriad of problems such as undesirable film morphologies, aggregation of the emitter as

K. Thakur, B. van der Zee, O. Sachnik, C. Haese, R. Graf, J. J. Michels, G.-J. A. H. Wetzelaer, C. Ramanan, P. W. M. Blom  
Department of Molecular Electronics  
Max Planck Institute for Polymer Research  
Ackermannweg 10, Mainz 55128, Germany  
E-mail: blom@mpip-mainz.mpg.de

 The ORCID identification number(s) for the author(s) of this article can be found under <https://doi.org/10.1002/adpr.202400022>.

© 2024 The Author(s). Advanced Photonics Research published by Wiley-VCH GmbH. This is an open access article under the terms of the Creative Commons Attribution License, which permits use, distribution and reproduction in any medium, provided the original work is properly cited.

DOI: 10.1002/adpr.202400022

well as unintentional interactions between the host and emitter.<sup>[15]</sup> In an effort to overcome these problems, various directions have been explored and two of such potential routes include TADF polymers and dendrimers. TADF dendrimers are from size point of view in between small molecules and polymers, where the TADF active part is a small molecule, but with large sidechains (dendrons) attached to it.<sup>[5,15]</sup> In TADF polymers, the TADF active group, often a small molecule, is introduced either in the main chain, or as a pendant group in a linear polymer.<sup>[16]</sup> The highest EQE obtained for a solution-processable TADF polymer with orange-greenish emission is 20% by Yang et al.<sup>[17]</sup> Similar values were obtained for solution-processed dendrimer-based TADF OLEDs, where a highest EQE of around 24% was obtained by Ban et al. for blue- and green-emitting OLEDs.<sup>[18]</sup> Both approaches (TADF polymers and dendrimers) are promising routes toward solution processability of TADF emitters, however their design structure is limited by a complex synthesis, and especially for TADF polymers, the existence of left-over impurities from the synthesis.<sup>[19]</sup> Moreover, the EQEs of TADF OLEDs based on polymer and dendrimers are still lower as compared to small-molecule-based TADF emitters.

Another approach is to make the small molecules themselves more amenable to solution processing. In 2014, Cho et al. developed highly efficient green solution-processable OLED based on the small-molecule 4CzIPN with an EQE of 18%. Here, the carbazole moieties of the molecules were modified with a *tert*-butyl group to improve the solubility.<sup>[20]</sup> Other moieties like methyl and other alkyl group have also been explored to improve the solubility of TADF emitters, but the *tert*-butylation has so far resulted in the highest efficiencies of solution-processed devices.<sup>[21]</sup>

*Tert*-butyl substitution has been widely used to make organic materials soluble, accompanied by good film formation. Xie et al.<sup>[22]</sup> reported blue heterodonor solution-processable blue TADF emitters, giving OLEDs with an EQE as high as 26%. The authors ascribed the high EQE to the highly twisted heterodonor configuration, which was achieved by *tert*-butylation. Similarly, in an another study by Shi et al. using *tert*-butyl-substituted donor and acceptor TADF emitters OLEDs with 20% EQE were realized.<sup>[23]</sup> The improved device performance of *tert*-butyl-substituted TADF emitters<sup>[24]</sup> is often attributed to a plethora of causes, including reduced nonradiative decay, reduced nonradiative self-quenching coming from bimolecular annihilation processes, but also to reduction in defects which lead to charge trapping.<sup>[25–27]</sup> Despite the abundantly reported positive effects of *tert*-butylation, a photophysical study quantifying the effect of *tert*-butylation by modeling the photoluminescence (PL) decays of TADF emitters is presently lacking. Such an investigation would be beneficial for the design of future solution-processable TADF materials.

In this work, the impact of *tert*-butyl substitution on the photophysical properties has been studied in a previously reported blue TADF emitter, consisting of a carbazole donor and a fluorine-substituted triazine acceptor in 9,9',9''-(5-(4,6-bis(4-fluorophenyl)-1,3,5-triazine-2-yl)benzene-1,2,3-triyl)tris(9-*H*-carbazole) (**3CzTrz-F**), and the *tert*-butylated variant 9,9',9''-(5-(4,6-bis(4-fluorophenyl)-1,3,5-triazine-2-yl)benzene-1,2,3-triyl)tris(3,6-di-*tert*-butyl-9-*H*-carbazole), referred to as **t3CzTrz-F** in this study.

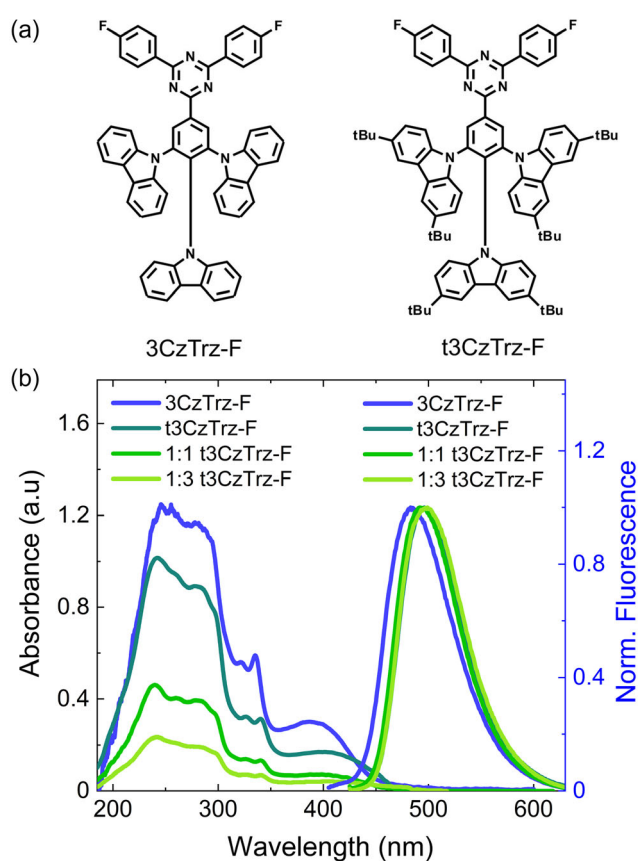


**Figure 1.** a) Chemical structure of **3CzTrz-F** and *tert*-butyl-substituted **t3CzTrz-F**. b) Absorption spectrum of solution-processed neat film of **3CzTrz-F** and **t3CzTrz-F** in blue and green, respectively; and 1:1 and 1:3 dilution of **t3CzTrz-F** in PS in the gradient of green color, respectively (left vertical axis). The spectra on the right side represent the steady-state emission of neat films of **3CzTrz-F** and **t3CzTrz-F**, respectively, as well as of the 1:1 and 1:3 blend of **t3CzTrz-F**:PS (right vertical axis).

The molecular structures of both TADF emitters are shown in **Figure 1a**. In addition, we study the effect of addition of a wide bandgap host on the photophysical properties of our **t3CzTrz-F** films.

We find that *tert*-butylation enhances the PL quantum yield (PLQY) in our **t3CzTrz-F** emitter as compared to the non-*tert*-butylated variant **3CzTrz-F**. Dilution of **t3CzTrz-F** in polystyrene (PS) increases the PLQY even up to 100%. The photophysical properties are characterized using steady-state (PLQY) and time-resolved PL (TRPL) spectroscopy, the latter in combination with kinetic rate equations, where we use the nonradiative decay of triplets to account for a PLQY that differs from 100%. Our results reveal that the addition of a *tert*-butyl group on the Cz donor moiety increases the rISC rate by about a factor of 4 and decreases the nonradiative triplet decay constant, consistent with the observed change in PLQY. The enhanced PLQY by diluting **t3CzTrz-F** in PS is associated with a further decreasing nonradiative decay constant in addition to an increase in singlet lifetime, while rISC remains the same. We employ solid-state NMR in order to rationalize these effects. Our study shows that *tert*-butylation enhances the photophysical properties

of TADF emitters, and our insights contribute to realizing efficient solution-processable TADF materials for low-cost fabrication.

## 2. Results

### 2.1. Steady-State Absorption and PL

Figure 1 shows the chemical structure of **3CzTrz-F** and **t3CzTrz-F** along with their steady-state absorption and emission spectra in a neat film with a thickness of 100 nm. Details on the synthesis are given in the Supporting Information. The absorption band in the shorter wavelength region (200–300 nm) is assigned to the  $\pi-\pi^*$  from the aromatic rings including the acceptor and donor units. The absorption bands between 290 and 330 nm are associated with  $n-\pi^*$  absorption peaks of the Cz moiety.<sup>[28–30]</sup> The lower energy transition extending from 355 nm to 450 nm is assigned to the singlet charge transfer (CT) band arising from the interaction of the electron donating Cz with the electron accepting Trz. This CT band is responsible for the TADF emission.<sup>[31]</sup> The emission spectrum of **3CzTrz-F** in the neat film exhibits a peak at 490 nm and yields a blue–green color. The emission spectrum of the *tert*-butyl-substituted **t3CzTrz-F** is slightly redshifted, exhibiting a peak at 505 nm.

### 2.2. Transient Photoluminescence

Figure 2 shows that both **3CzTrz-F** and **t3CzTrz-F** exhibit TADF, verified by the temperature-dependent delayed emission observed in TRPL. The double logarithmic plot of PL intensity versus time shows the characteristic kinetic decay curve, consisting of a prompt and a delayed fluorescence component. The prompt component originates from fluorescence of optically generated singlets that have not undergone any other cycling process, whereas the delayed component is fluorescence of generated singlets that were transferred to the triplet state by ISC and subsequently have come back to the singlet state through rISC. As rISC is a temperature-activated process, the delayed component shows a temperature dependence, strongly reducing the contribution of TADF from 295 to 77 K. We observe that the line shape of the delayed component of the **3CzTrz-F** film is different from that of the **t3CzTrz-F** film, as can be seen in Figure 2a,b. There is a reduction in lifetime for the **t3CzTrz-F** films, as well as a more evenly spaced temperature dependence. Furthermore, a sharper transition between prompt and delayed fluorescence can be seen at 77 K. The **t3CzTrz-F** retains its line shape for the prompt region in dilution with a PS host (Figure 2c,d), whereas the delayed lifetime does show an increase for the blended films.

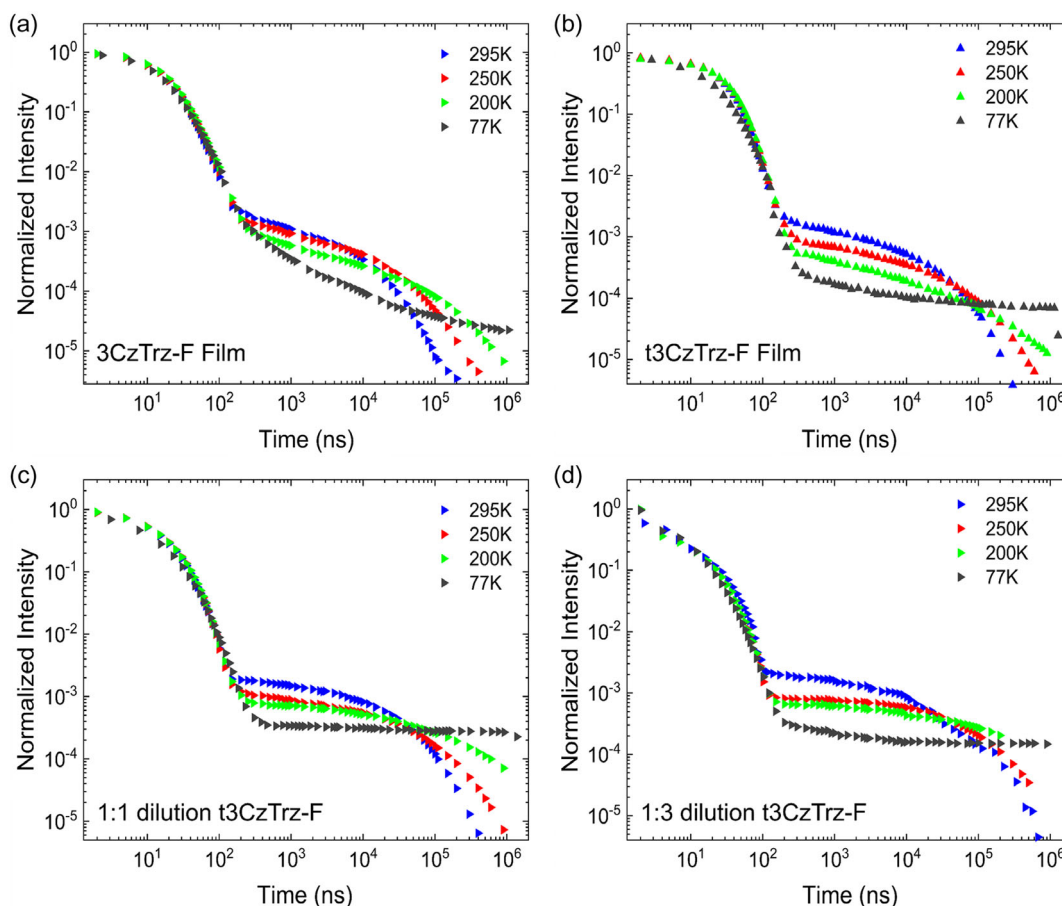


**Figure 2.** Temperature scan of transient photoluminescence spectra of a,b) the neat film of **3CzTrz-F** and **t3CzTrz-F** and c,d) diluted film of **t3CzTrz-F** in polystyrene host.

### 2.3. Transient PL Modeling

To determine the effect of *tert*-butylation on the photophysical properties, we also carried out excitation intensity dependent TRPL measurements on neat films of **3CzTrz-F** and **t3CzTrz-F**. In a previous publication, we demonstrated how kinetic modeling can be used to reliably extract photophysical rate constants from TRPL curves.<sup>[32]</sup> In addition, it was shown that modeling TRPL data at various incident laser powers can be used to estimate the rate constants of bimolecular processes such as triplet-triplet annihilation (TTA).<sup>[32]</sup> For completeness and as it forms the basis for the model used in this work, we will shortly revisit the kinetic model here. The singlet and triplet populations take the form of linear differential equations

$$\frac{d[S]}{dt} = \frac{[S_0]}{dt} - \frac{[S]}{\tau_s} - k_{\text{ISC}}[S] + k_{\text{rISC}}[T] + 0.25k_{\text{TTA}}[T][T] \quad (1)$$

$$\frac{d[T]}{dt} = k_{\text{ISC}}[S] - k_{\text{rISC}}[T] - 1.25k_{\text{TTA}}[T][T] \quad (2)$$

where  $[S_0]$  is the initial singlet density, determined from the absorption of the emitter.<sup>[32]</sup> The second term on the right-hand side (Equation (1)) corresponds to monomolecular decay of singlets, i.e., fluorescence, determined by  $\tau_s$ , the lifetime of singlets.  $k_{\text{ISC}}$  is the (reverse) intersystem crossing rate constant and  $k_{\text{TTA}}$  is the TTA rate constant. Note that the intrinsic triplet lifetime of the TADF emitter is assumed to be infinite.

These equations are solved numerically using the finite difference method.

To estimate the annihilation effects, we first investigated the power dependence on neat films (**Figure 3**). We see almost no power dependence in the TRPL data for both **3CzTrz-F** and **t3CzTrz-F**. This suggests that the contribution of excitation density-dependent processes, such as singlet-triplet and triplet-triplet annihilation ( $k_{\text{STA}}$  and  $k_{\text{TTA}}$ ), are negligible.<sup>[32]</sup> Therefore, we neglect these contributions in the rate equation. However, Equation (1) and (2) implicitly assume that the PLQY of the emitter is 100%, which means there is no nonradiative decay. This might be valid for some emitters;<sup>[33]</sup> however, this is not the case for the **3CzTrz-F** emitters used in this work. In **Table 1**, we show the calculated values of the exciton density along with the

**Table 1.** PLQY and initial singlet density of for the **3CzTrz-F**, **t3CzTrz-F** and **t3CzTrz-F** in the host polystyrene in 1:3 dilution. The value of PLQY is determined experimentally measuring the PL emission nitrogen environment. The initial singlet density calculated using the formula given in ref. [6].

	3CzTrz-F	t3CzTrz-F	1:3 t3CzTrz-F
PLQY [%]	46	80	100
$S_0$ [ $\text{m}^{-3}$ ]	$3.3 \times 10^{23}$	$2.6 \times 10^{23}$	$7.0 \times 10^{22}$

experimentally determined PLQY for both emitters. We see that adding the *tert*-butyl groups increases the PLQY substantially, from 46% to 80%, which further increases to 100% in the 1:3 dilution film in a PS host. To take this effect of PLQY into account, a nonradiative decay constant of  $-k_{\text{nrT}}[T]$  is added to the triplet rate equation (Equation (2)), where  $k_{\text{nrT}}$  is the nonradiative decay constant of triplets. The short effective singlet lifetime originating from a fast ISC rate usually means that the nonradiative decay of singlets is less significant than the nonradiative decay of the longer living triplets.<sup>[34]</sup> Therefore, in order to limit the number of fitting parameters, we omit the nonradiative decay of singlets. Thus, the simplified equations without TTA and considering nonradiative triplet decay become

$$\frac{d[S]}{dt} = \frac{[S_0]}{dt} - \frac{[S]}{\tau_s} - k_{\text{ISC}}[S] + k_{\text{rISC}}[T] \quad (3)$$

$$\frac{d[T]}{dt} = +k_{\text{ISC}}[S] - k_{\text{rISC}}[T] - k_{\text{nrT}}[T] \quad (4)$$

The TRPL decay curves of neat films of **3CzTrz-F** and **t3CzTrz-F** are plotted in **Figure 4**, where the most noticeable difference between the two curves is the point of transition from prompt fluorescence (PF) to delayed fluorescence (DF). Modeling the TRPL curves of **3CzTrz-F** and **t3CzTrz-F** leads to the fits in **Figure 4** with the parameters presented in **Table 2**. The low power density of  $8 \text{ mW cm}^{-2}$  ensures that bimolecular annihilation does not play a large role. The modeling (**Table 2**) reveals that the addition of the *tert*-butyl group yields two significant contributions to the photophysical characteristics.

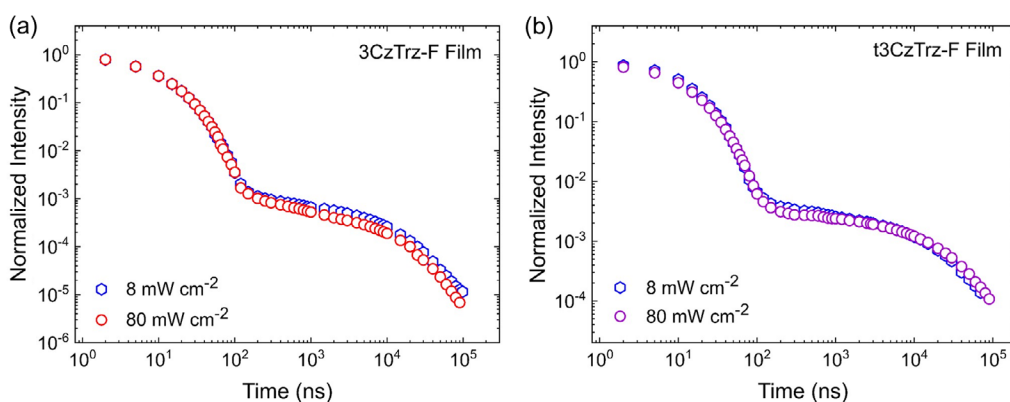


**Figure 3.** Normalized transient PL curves of a) **3CzTrz-F** film and b) **t3CzTrz-F** film at different power densities. Open symbol represents the measured data. Kinetic curves at 8 and  $80 \text{ mW cm}^{-2}$  are both on top of each other for the both the cases of **3CzTrz-F** and **t3CzTrz-F** films.

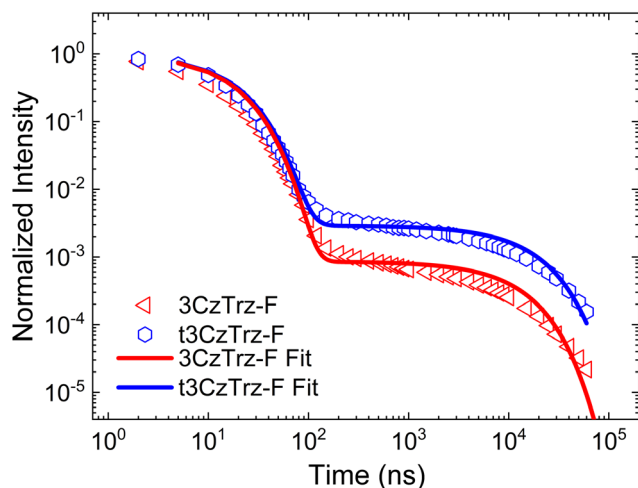


**Figure 4.** Transient PL curves of neat **3CzTrz-F** and **t3CzTrz-F** films at the excitation density of  $8 \text{ mW cm}^{-2}$  shown in circle symbol in red and blue, respectively. The line in red and blue represents the fit obtained from the kinetic modelling of the PL curves.

**Table 2.** Summary of photophysical parameters determined from the kinetic fitting of the transient kinetic curves of **3CzTrz-F** and **t3CzTrz-F** measured at an incident excitation power of  $8 \text{ mW cm}^{-2}$ .

	<b>3CzTrz-F</b>	<b>t3CzTrz-F</b>
$S_0 [\text{m}^{-3}]$	$3.3 \times 10^{23}$	$2.6 \times 10^{23}$
$\tau_s [\text{ns}]$	65	90
$k_{\text{nrT}} [\text{s}^{-1}]$	$5.7 \times 10^4$	$1.4 \times 10^4$
$PLQY_{\text{fit}} [\%]$	46	80
$k_{\text{ISC}} [\text{s}^{-1}]$	$3.8 \times 10^7$	$4.0 \times 10^7$
$k_{\text{rISC}} [\text{s}^{-1}]$	$6.4 \times 10^4$	$1.9 \times 10^5$

First, the value of  $k_{\text{nrT}}$  is decreased by a factor of 4 upon *tert*-butylation. Second, there is an enhancement in  $k_{\text{rISC}}$  by about a factor of 3.4. Furthermore, the PLQY calculated using the  $k_{\text{nrT}}$  extracted from the modeling (Table 2) is in agreement with the experimentally observed PLQY values (Table 1). The increase in  $k_{\text{rISC}}$  found in the **t3CzTrz-F** emitter is exactly what causes the transition region between PF and DF to move up, as compared to **3CzTrz-F**, which can be seen in Figure 4. The increase in  $k_{\text{rISC}}$  changes the competitive balance between  $k_{\text{rISC}}$  and  $k_{\text{nrT}}$ , automatically leading to less nonradiative decay events. Besides the shift in decay pathways for triplets, also the decrease in  $k_{\text{nrT}}$  itself is responsible for the increase in PLQY. Decreasing the nonradiative decay of triplets is important for OLEDs because electrically triplets are generated in a 3:1 ratio compared to singlets. As noted before,<sup>[34]</sup> calculating the EQE of an OLED using the value of the PLQY is not entirely correct when a large portion of triplets in the TADF emitter decays nonradiatively. Rather, one should correct for the initial 1:3 ratio of singlet:triplet, where electrically the effect of  $k_{\text{nrT}}$  is naturally larger than in optical experiments.<sup>[34–36]</sup>

As stated previously, TADF materials are often diluted within a wide bandgap host in order to reduce concentration quenching.

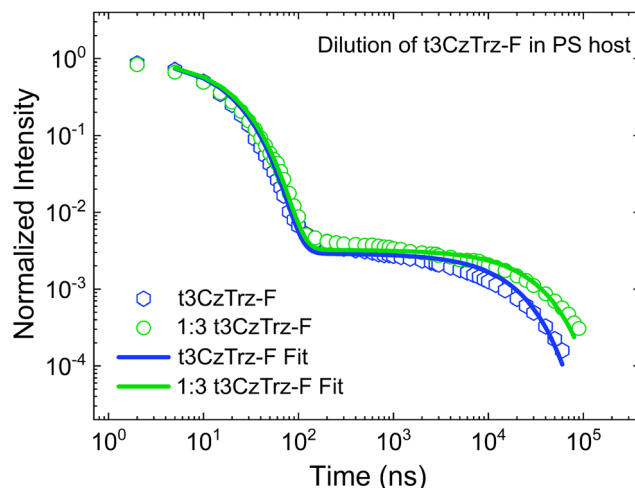


**Figure 5.** Transient PL curves of neat **3CzTrz-F** and 1:3 diluted **t3CzTrz-F** films in polystyrene ratio at the excitation density of  $8 \text{ mW cm}^{-2}$  shown in circle symbol in red and blue, respectively. The line in red and blue represents the fit obtained from the kinetic modelling of the PL curves.

As a next step we investigate the effect of this on **t3CzTrz-F**. We observe that the dilution of **t3CzTrz-F** in PS further increases the PLQY value, from 80% to 100%, as shown in Table 1. We investigate the photophysical parameters of **t3CzTrz-F** diluted in the PS host in a 1:3 ratio (Figure 5). The extracted photophysical parameters are summarized in Table 3. Figure 5 shows the transient PL curve of the **t3CzTrz-F** and 1:3 **t3CzTrz-F** film at a power density of  $8 \text{ mW cm}^{-2}$ , where we see that the PF is on top of each other, but the later part of the DF tail is higher in the diluted film. Modeling of these kinetic curves reveals that both the ISC and rISC are the same in both the cases; however,  $k_{\text{nrT}}$  changes. There is no detectable nonradiative decay in the 1:3 diluted film and  $k_{\text{nrT}}$  substantially decreases from  $1.4 \times 10^4 \text{ s}^{-1}$  in the pristine **t3CzTrz-F** film to a value no larger than  $1 \times 10^1 \text{ s}^{-1}$  in the 1:3 **t3CzTrz-F** diluted film, implying that it is small enough not to affect the delayed fluorescence lifetime. Moreover, the singlet lifetime increases from 90 to 120 ns, which could indicate a reduction of nonradiative singlet decay as well. However, as stated before, nonradiative singlet decay was neglected in our modeling because a fast ISC rate overshadows its impact, making the impact of  $k_{\text{nrT}}$  on the total exciton population more significant. In turn, this results in complete rISC of

**Table 3.** Summary of photophysical parameters obtained by the kinetic fitting of TrPL decay of neat **3tCzTrz-F** and 1:3 diluted **3tCzTrz-F** film in a PS host.

	<b>t3CzTrz-F</b>	<b>1:3 t3CzTrz-F</b>
$S_0 [\text{m}^{-3}]$	$2.6 \times 10^{23}$	$7.0 \times 10^{22}$
$\tau_s [\text{ns}]$	90	120
$PLQY [\%]$	80	100
$k_{\text{nrT}} [\text{s}^{-1}]$	$1.4 \times 10^4$	$<1.0 \times 10^1$
$k_{\text{ISC}} [\text{s}^{-1}]$	$4.0 \times 10^7$	$4.0 \times 10^7$
$k_{\text{rISC}} [\text{s}^{-1}]$	$1.9 \times 10^5$	$1.9 \times 10^5$

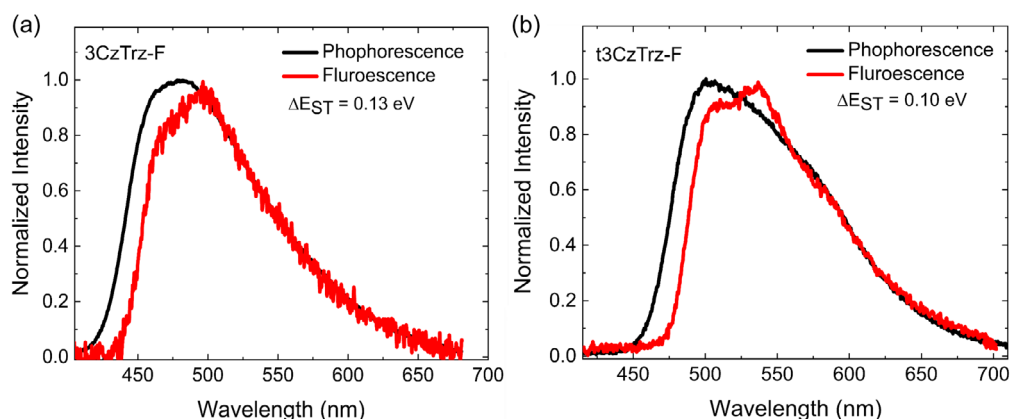


**Figure 6.** Emission spectra of fluorescence measured at room temperature in black and phosphorescence measured at 10 k for a) **3CzTrz** and b) **t3CzTrz-F** films.

triplet excitons, rationalizing the 100% PLQY. Additionally, we see that the intrinsic singlet lifetime also slightly increases in case of the diluted film.

**Figure 6** shows the fluorescence spectra measured at 295 K, together with the phosphorescence spectra measured at 10 K. As the phosphorescence spectrum shows vibronic features, the singlet–triplet splitting ( $\Delta E_{ST}$ ) calculation is done by fitting the slope of the onset of the emission, which leads to ( $\Delta E_{ST}$ ) values of 0.13 and 0.10 for **3CzTrz-F** and **t3CzTrz-F**, which is consistent with the earlier reported value for compounds similar to **3CzTrz-F** (note that this method can have an error margin which approaches the observed difference in the  $\Delta E_{ST}$  values for the two TADF molecules). The change in  $\Delta E_{ST}$  can influence the change observed in the  $k_{rISC}$ ; however, it does not explain the observed reduction in  $k_{nr}$ . To further confirm the origin of enhanced photophysical parameters, a solid-state NMR study is done to study the impact molecular geometry on the photophysical properties.

## 2.4. Solid-State NMR

To gain a better understanding of the process that reduces the nonradiative decay rate upon introducing *tert*-butyl groups to the TADF system, it is essential to take a closer look at the organization and dynamics of the TADF molecules in the solid state. Here, magic angle spinning (MAS) NMR spectroscopy can provide detailed information about dynamic processes of the

corresponding compounds in the pure sublimated sample, as well as in a binary mixture with PS. Common methods used here are the determination of  $^{19}\text{F}$   $T_1$  relaxation times by saturation recovery experiments probing dynamic processes with correlation times at the Larmor frequency and the determination of dipolar coupling constants of C–H pairs with the REPT-HDOR pulse sequence probing molecular motion with correlation times in the kHz–MHz range. In order to assign the determined dynamic parameters to the respective atomic sites of the chemical structure, it is first necessary to perform a complete structure elucidation of the molecules with a full assignment of all spectrally resolved resonances. The results of this analysis with the assignment of all  $^1\text{H}$  and  $^{13}\text{C}$  signals are given in the Supporting Information.

The determined  $^{19}\text{F}$   $T_1$  relaxation times of compounds **3CzTrz-F** and **t3CzTrz-F** and their mixtures with PS are shown in **Table 4**. It is worth noting that the molecular symmetry, where the two fluorine sites in the molecules are equivalent, is typically broken for molecules in the solid state due to different local environments of the fluorine atoms, which appear as distinct chemical shifts in the  $^{19}\text{F}$  MAS NMR spectrum.

The neat sample **t3CzTrz-F** shows five different  $^{19}\text{F}$  signals (**Figure 7a**). These signals can be assigned to two different phases, amorphous and crystalline, which was done using single pulse as well as double quantum filtered  $^{19}\text{F}$  correlation spectra as well as  $^{19}\text{F}\{^1\text{H}\}$  CP-HETCOR (more detailed shown in **Figure S1** and **S2**, Supporting Information).

**Table 4.**  $^{19}\text{F}$   $T_1$  relaxation times for **t3CzTrz-F** and **3CzTrz-F** and their respective mixtures with polystyrene.

Pure TADF material				TADF material in polystyrene			
<b>t3CzTrz-F</b>		<b>3CzTrz-F</b>		<b>t3CzTrz-F</b>		<b>3CzTrz-F</b>	
Chemical shift [ppm]	$T_1$ time [s]	Chemical shift [ppm]	$T_1$ time [s]	Chemical shift [ppm]	$T_1$ time [s]	Chemical shift [ppm]	$T_1$ time [s]
−100.6	2.5	−101.0	25	−105.0	13.3	−100.8	25
−103.0	2.8	−108.3	28	–	–	−102.7	32
−105.2	0.5/1.8	–	–	–	–	−104.3	15/90
−106.3	0.6/2.1	–	–	–	–	−107.6	29
−107.4	0.7/2.0	–	–	–	–	−110.1	18

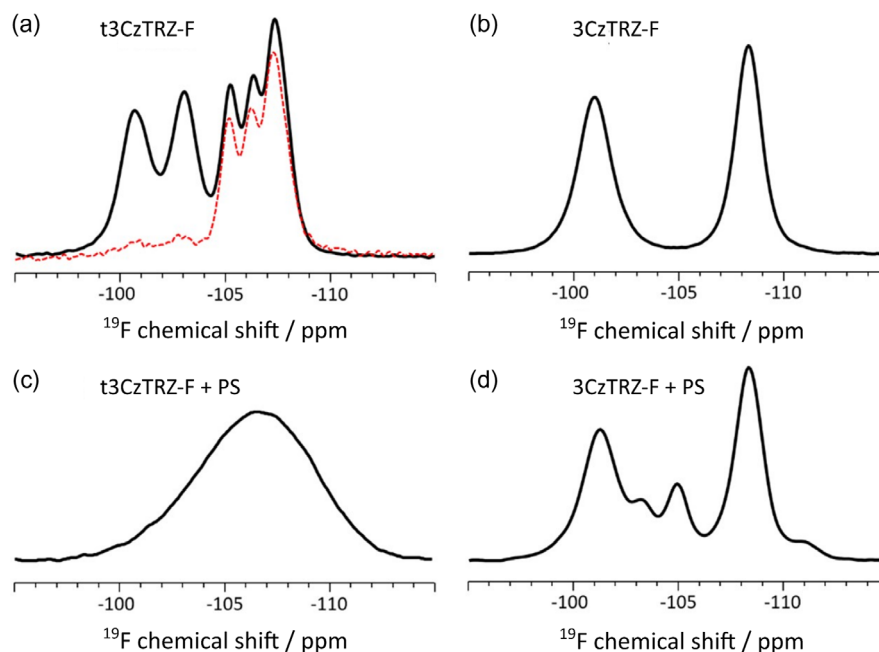


**Figure 7.**  $^{19}\text{F}$  MAS spectra of a)  $t3\text{CzTrz-F}$ , b)  $3\text{CzTrz-F}$ , and c,d) their respective mixtures with polystyrene, measured at a rotation frequency of 25 kHz.

For the two broader signals at lower field (Figure 7a, two left peaks), the  $^{19}\text{F}$   $T_1$  relaxation times of about 2.6 s are significantly longer than the relaxation times of the other three sharper signals. However, their  $T_1$  relaxation times of 2.5 and 2.8 s, respectively, are in a range in which amorphous or nanocrystalline materials with a high internal mobility of the individual molecular fragments are observed. The extinction of these two signals after the use of a double quantum filter indicates that the fluorine atoms are not in close spatial proximity ( $<0.5$  nm). However, the other three signals show double-quantum coherences, suggesting that this phase has much denser packing of the molecules, which results from the fact that both translational and rotational motion can be strongly limited by the steric demand of the *tert*-butyl groups in the crystal lattice.

The signals of the fluorine atoms in the crystalline phase, spanning from  $-105.2$  to  $-107.4$  ppm (Figure 7a), show a biexponential  $T_1$  relaxation behavior. Here, the shorter relaxation time was determined to be in the range of hundreds of milliseconds, while the slower relaxing component shows a behavior comparable to the relaxation processes determined for the non-crystalline phase. Usually  $T_1$  relaxation times in rigid crystalline morphologies are significantly longer, compared to those in noncrystalline regions. In this special case, however, dynamic processes of the *tert*-butyl groups located in close spatial proximity to the fluorine atoms, which is ensured by the crystalline packing, lead to their very short  $T_1$  relaxation time (see Section S3 and S4, Supporting Information). The biexponential time dependence of the  $T_1$  relaxation for both  $^1\text{H}$  and  $^{19}\text{F}$  SS-NMR signals in the crystalline environment is in full agreement with the common relaxation theory and known from the literature for cases where the  $T_1$  relaxation is driven by strong  $^1\text{H}$ - $^{19}\text{F}$  heteronuclear dipolar couplings and one of the spin species shows a dynamic process around a local  $C_3$  symmetry axis.<sup>[37]</sup> In contrast,  $3\text{CzTrz-F}$

without *tert*-butyl groups shows only two signals in the  $^{19}\text{F}$  MAS spectrum (Figure 7b). The  $^{19}\text{F}$   $T_1$  relaxation times are almost an order of magnitude higher than those of the compound  $t3\text{CzTrz-F}$ , which we attribute to the lacking perturbation by the rotation processes of the aliphatic units in the materials.

Mixing the two compounds with PS leads to changes in chemical shifts, number of signals, and  $T_1$  relaxation times. For the compound  $t3\text{CzTrz-F}$ , only one broad, featureless  $^{19}\text{F}$  NMR signal was detected (Figure 7c). For this signal, a single  $T_1$  relaxation time of 13.3 s was determined. This can be explained by the good miscibility of the TADF molecules with PS. The dispersion of the TADF molecules in PS removes the ordering of the molecules in the crystalline phase, indicated by the loss of the five different resonances and resulting in a spatial separation between  $^{19}\text{F}$  sites and *tert*-butyl groups. The absence of the rotating aliphatic group in close proximity to the fluorine atoms leads to a longer  $T_1$  relaxation time.

After mixing with PS,  $3\text{CzTrz-F}$  shows five signals in the  $^{19}\text{F}$  MAS NMR spectrum (Figure 7d), whereby the two signals observed in the pure sample are retained. A quantitative analysis of the spectrum by fitting shows that the proportion of the initial morphology is  $\approx 80\%$ .

The two of the three new signals, at  $-102.7$  and at  $-110.1$  ppm, show a  $T_1$  relaxation behavior similar to the crystalline fraction, suggesting that these signals originate from the interface between the TADF crystallites and the PS matrix. The third new  $^{19}\text{F}$  signal shows a biexponential relaxation behavior, which may reflect the dynamic heterogeneity in the sample. The  $^{19}\text{F}$ - $^{19}\text{F}$  back-to-back correlation spectra of  $3\text{CzTrz-F}$  in PS show no correlation involving the newly formed species. This suggests that the  $3\text{CzTrz-F}$  molecules in the PS matrix are most likely isolated or mobile on the millisecond time scale so that double-quantum coherences cannot be excited.

In order to monitor molecular dynamics on micro- to millisecond time scales, the C–H heteronuclear dipolar coupling for both the pure compounds and the mixtures with PS has been determined and will be discussed. The data for this procedure were extracted from REPT-HDOR experiments,<sup>[38]</sup> with which dipolar rotational sideband patterns for the particular carbon atoms can be identified. Here, we will consider the primary carbon atoms of the carbazole units, which are oriented toward the central phenyl ring. Assuming a Gaussian distribution of thermal molecular fluctuations, fitting of the residual dipolar couplings  $D_{\text{exp}}$  yields the width  $2\sigma$  of the distribution of the molecular fluctuations. Comparing the determined dipolar coupling constants  $D_{\text{exp}}$  with the rigid case  $D_0$ , depending exclusively on the distance between the  $^{13}\text{C}$  and the  $^1\text{H}$  nuclear spin, provides the dynamic order parameter that is described by  $S = \frac{D_{\text{exp}}}{D_0}$ . An order parameter  $S = 1$  indicates the fully rigid case, while the amplitude of molecular fluctuations increases with decreasing values of  $S$ . A value of  $S = 0$  corresponds to fully isotropic molecular fluctuations. It should be pointed out that the dynamic order parameter  $S$  describes the time averaged behavior of a molecular orientation, and therefore deviates from the ensemble averaged order parameter known from liquid crystalline systems in nonergodic systems. The determined dipolar coupling constants  $D$ , the resulting dynamic order parameter  $S$ , and the width  $2\sigma$  of Gaussian molecular fluctuations are summarized in **Table 5**.

In the crystalline environment of the neat TADF materials, no molecular fluctuations of the carbazole units are observed. When the TADF molecules are incorporated into a PS matrix, the mobility of the donor fragments clearly changes. Here, **t3CzTrz-F** is most affected with larger angle molecular fluctuations of  $2\sigma = 47^\circ$  width. In the case of **3CzTrz-F**, this width of the distribution increases to only  $15^\circ$ . This value has to be taken with care, as the REPT-HDOR method cannot distinguish between molecules in the crystalline environment and those dispersed in the polymer matrix.<sup>[39]</sup> The SS-NMR observations clearly indicate a good miscibility for the *tert*-butylated TADF material with PS, while for the non-*tert*-butylated material a formation of phase separated crystals occurs. For the neat **t3CzTrz-F** material, we observed two phases after solution processing, which we address to a noncrystalline and a crystalline morphology. Here, the noncrystalline phase shows a high mobility of the molecules or an irregular packing of the fluorine sites, so that no double-quantum resonances were found. The crystalline material shows shorter relaxation times than the noncrystalline phase, mainly caused by the spatial proximity of the *tert*-butyl groups and fluorine sites due to a regular dense packing. Most importantly, the aliphatic groups lead to an enlarged spacing between the TADF molecules,

**Table 5.** Dipolar C–H coupling constants, order parameters and fluctuation angles for the carbazole units of **t3CzTrz** and **3CzTrz** and their respective mixtures with polystyrene.

Pure TADF material			TADF material in polystyrene								
t3CzTrz-F			3CzTrz-F			t3CzTrz-F			3CzTrz-F		
$D$ [kHz]	$S$	$2\sigma$	$D$ [kHz]	$S$	$2\sigma$	$D$ [kHz]	$S$	$2\sigma$	$D$ [kHz]	$S$	$2\sigma$
21.5	1.00	$0^\circ$	21.5	1	$0^\circ$	17.2	0.8	$47^\circ$	21.0	0.98	$15^\circ$

thus reducing the electronic couplings between neighboring molecules, which results in an improved photoluminescence behavior compared to **3CzTrz-F**. The mixing of the TADF molecules with PS leads to even larger spatial separation between the molecules. However, only **t3CzTrz-F** blends homogeneously with the polymer matrix, while an 80% fraction of **3CzTrz-F** retains in its pure crystalline state. Therefore, it is not surprising that the blend of **t3CzTrz-F** shows an increase in the PL efficiency.

## 2.5. Connecting NMR and Photophysical Results

The solid-state NMR results give insight in the morphological reasons underlying our photophysical results. For **t3CzTrz-F**, there are two features that contribute to the decreasing  $k_{\text{nrT}}$  as compared to **3CzTrz-F**. First, the enlarged spacing caused by the *tert*-butyl groups decreases the coupling between neighboring units. Second, a certain fraction of the **t3CzTrz-F** neat film shows a denser and more crystalline packing, corroborated by the dynamic order parameter  $S$  becoming unity, which corresponds to a fully rigid case. The rigidity means a reduction of vibrational motion, which directly explains the less nonradiative triplet decay.<sup>[40–42]</sup> Previous work had suggested that rigidity increases exciton diffusion, which could lead to emission quenching.<sup>[43]</sup> Additional emission quenching coming from exciton diffusion would lead to a reduction of the PLQY, this is in contrast our PLQY results, which show an increase instead, suggesting that this mechanism does not play a significant role. Moving to the **t3CzTrz-F:PS** blend, the SS-NMR results indicate a good miscibility between the two constituents. From the NMR data we see no further rigidification when blending **t3CzTrz-F** with the PS host, thus the further decrease of  $k_{\text{nrT}}$  can be explained solely by the enlarged spacing between the TADF molecules, in accordance with previous work.<sup>[44]</sup>

Next, we also observe that *tert*-butylation of **3CzTrz-F** gives rise to an increase in  $k_{\text{rISC}}$ . It is known that the steric hindrance coming from the *tert*-butyl group in our case can restrict the rotational motion around the donor–acceptor (D–A) angle,<sup>[45]</sup> which for **3CzTrz-F** was found to be around  $120^\circ$ .<sup>[24]</sup> Controlling molecular conformation and in particular rigidification of TADF molecules has been shown to be a favorable route toward optimized TADF emitters.<sup>[46,47]</sup> Previous work has suggested that more rigid molecular structures tend to have a lower  $\Delta E_{\text{ST}}$ .<sup>[42]</sup> It does require a balance however because at the same time large steric hindrance has shown to lead to the deactivation of TADF altogether.<sup>[45]</sup> Most likely driven by the denser packing (as from the SS-NMR results), a more orthogonal D–A angle leads to a lower  $\Delta E_{\text{ST}}$ , higher  $k_{\text{rISC}}$ , and higher  $\tau_{\text{s}}$ . Assuming ISC and rISC to be in equilibrium, their ratio can be expressed as<sup>[40]</sup>

$$\frac{k_{\text{rISC}}}{k_{\text{ISC}}} = \frac{1}{3} \exp\left(\frac{-\Delta E_{\text{ST}}}{k_{\text{B}} T}\right) \quad (5)$$

Considering the experimental values of  $\Delta E_{\text{ST}}$ , 0.13 for **3CzTrz-F** and 0.10 for **t3CzTrz-F**, and using Equation (5),  $k_{\text{rISC}}$  should increase from  $6.4 \times 10^4 \text{ s}^{-1}$  to around  $2.1 \times 10^5 \text{ s}^{-1}$  when  $\Delta E_{\text{ST}}$  changes from 0.13 to 0.10. This predicted value of  $k_{\text{rISC}}$  is close to the modeled value of  $1.9 \times 10^5 \text{ s}^{-1}$ , indicating that the change  $\Delta E_{\text{ST}}$  is the main driver behind the increase in  $k_{\text{rISC}}$ .



It is worth mentioning that previous work showed that controlling the spatial overlap between highest occupied molecular orbital and lowest unoccupied molecular orbital, as is done by changing the D–A angle, in fact leads to less nonradiative singlet decay.<sup>[44]</sup> While this is not taken into account in our analysis, we cannot exclude that it contributes to the increased PLQY of **t3CzTrz-F** as well.

### 3. Conclusion

In this work, we study the photophysical properties of *tert*-butylation on a blue TADF emitter. We find through modeling of the TrPL curves that adding a *tert*-butyl group is associated with two positive effects: it increases the value of rISC and it reduces the nonradiative triplet decay constant. By diluting our *tert*-butylated emitter in a PS host, we are able to obtain 100% PLQY, i.e., completely suppress the nonradiative triplet decay. To rationalize our findings, we complement our photophysical study with solid-state NMR experiments, showing the relevance of molecular packing effects on nonradiative triplet decay and rISC rate. We expect the trend found in this study to continue for other materials, but the magnitude of this effect will likely vary between emitters. Structure–property relationships, like the one established in this article, are indispensable in the design of new high-performance and solution-processable TADF emitters.

### 4. Experimental Section

**Synthesis:** **3CzTrz-F** and **t3CzTrz-F** were synthesized in house as described in the Supporting Information.

**Sample Preparation:** All films for spectroscopic characterization (PLQY/TrPL/steady-state UV–vis–NIR) as well as NMR were prepared by spin coating the material onto a quartz substrate in a glovebox environment. The samples were then loaded into a home-built air-tight sample holder inside the glove box before transferring them outside for spectroscopic measurements.

**Spectroscopic Characterization:** Steady-state absorption was measured with a setup consisting of a deuterium halogen lamp (DH2000-DUV, OceanOptics) connected with a USB spectrometer (34 000-UV–vis–EIS, OceanOptics). Steady-state fluorescence was measured on a Horiba/Jobin Yvon Fluorolog-3 Spectrofluorometer. PLQY measurements were performed on a Horiba/Jobin Yvon Fluorolog-3, using an integrating sphere (F-3018) from Horiba while the samples were continuously flushed with nitrogen.

TRPL measurements were carried out using a 4Picos gated-iCCD camera (Stanford Computer Optics). Samples were photoexcited using the output from a Ti:sapphire laser (Coherent, Astrella, 1 kHz, 5 mJ, 35 fs) paired with a commercial optical parametric amplifier (Coherent, OperA). The spectra are collected using the 4Spec software (Stanford Computer Optics) using gating times ranging exponentially from 0.5 to 50 000 ns and spectra were recorded out to 50  $\mu$ s. The photoexcitation light was focused onto the sample in order to ensure a uniform excitation density throughout the film. The analysis of the TrPL data is done according to a previous study.<sup>[32]</sup>

**Solid-State NMR:** All solid-state NMR experiments shown here have been recorded on a Bruker Avance III NMR console operating at 500 MHz <sup>1</sup>H Larmor frequency using a commercial <sup>1</sup>H-<sup>19</sup>F-X MAS NMR probe supporting zirconia MAS rotors with 2.5 mm outer diameter. If not stated differently, the measurements have been performed at 25 kHz MAS spinning frequency and the rf nutation frequencies on all channels have been adjusted to 100 kHz, corresponding to a 90° excitation pulse length of 2.5  $\mu$ s. <sup>19</sup>F MAS NMR measurements have been recorded, with

a weak swf-TPPM <sup>1</sup>H decoupling (Rajendra Singh Thakur, Narayanan D. Kurur, P.K. Madhu, “Swept-frequency two-pulse phase modulation for heteronuclear dipolar decoupling in solid-state NMR”, Chem. Phys. Lett. 426, 459 (2006).) in order to obtain the optimal spectral resolution. The applied decoupling field strength was between 10 and 20 kHz and has been adjusted for every sample individually.

All T<sub>1</sub> relaxation measurements have been performed using the saturation recovery method, which leads to a higher uncertainty in the analysis of the experimental data compared to the inversion recovery method due to the undefined intensity for infinitely long relaxation times but at the same time allows for a proper handling of largely varying relaxation times often observed in partially crystalline compounds with <sup>19</sup>F nuclear spins as the results are independent of the repetition rate of subsequent transients. In between 20 to 50 90° pulses with changing time delays and phases have been applied to ensure reliable saturation of the initial polarization, while the delay between subsequent transients was kept short at 0.5 s. The analysis of the relaxation behavior has been performed using the Bruker Dynamic Center software version 2.4.10.

### Supporting Information

Supporting Information is available from the Wiley Online Library or from the author.

### Conflict of Interest

The authors declare no conflict of interest.

### Data Availability Statement

The data that support the findings of this study are available from the corresponding author upon reasonable request.

### Keywords

organic light-emitting diodes, thermally activated delayed fluorescence, photophysics, *tert*-Butylation

Received: February 5, 2024

Revised: May 11, 2024

Published online: June 19, 2024

- [1] H. Uoyama, K. Goushi, K. Shizu, H. Nomura, C. Adachi, *Nature* **2012**, 492, 234.
- [2] F. B. Dias, T. J. Penfold, A. P. Monkman, *Methods Appl. Fluoresc.* **2018**, 5, 012001.
- [3] N. B. Kotadiya, P. W. M. Blom, G.-J. J. A. H. Wetzelaer, *Nat. Photonics* **2019**, 13, 765.
- [4] Q. Zhang, D. Tsang, H. Kuwabara, Y. Hatae, B. Li, T. Takahashi, S. Y. Lee, T. Yasuda, C. Adachi, *Adv. Mater.* **2015**, 27, 2096.
- [5] Q. Wei, Z. Ge, B. Voit, *Macromol. Rapid Commun.* **2019**, 40, e1800570.
- [6] X. Cai, S. J. Su, *Adv. Funct. Mater.* **2018**, 28, 1802558.
- [7] D. Zhang, M. Cai, Y. Zhang, D. Zhang, L. Duan, *Horizons* **2016**, 3, 145.
- [8] L. Duan, L. Hou, T. W. Lee, J. Qiao, D. Zhang, G. Dong, L. Wang, Y. Qiu, *J. Mater. Chem.* **2010**, 20, 6392.
- [9] T.-W. Lee, T. Noh, H.-W. Shin, O. Kwon, J.-J. Park, B.-K. Choi, M.-S. Kim, D. W. Shin, Y.-R. Kim, *Adv. Funct. Mater.* **2009**, 19, 1625.
- [10] P. W. M. Blom, N. I. Craciun, D. M. De Leeuw, G. A. H. Wetzelaer, H. T. Nicolai, M. Kuik, *Adv. Mater.* **2014**, 26, 512.

- [11] Y. Zou, S. Gong, G. Xie, C. Yang, *Adv. Opt. Mater.* **2018**, *6*, 1800568.
- [12] K. Philipps, Y. Ie, B. van der Zee, R. Png, P. K. H. Ho, L. Chua, E. del Pino Rosendo, C. Ramanan, G. A. H. Wetzelaer, P. W. M. Blom, J. J. Michels, *Adv. Sci.* **2022**, *9*, 2200056.
- [13] S. Y. Lee, T. Yasuda, H. Komiyama, J. Lee, C. Adachi, *Adv. Mater.* **2016**, *28*, 4019.
- [14] H. J. Kim, C. Lee, M. Godumala, S. Choi, S. Y. Park, M. J. Cho, S. Park, D. H. Choi, *Polym. Chem.* **2018**, *9*, 1318.
- [15] T. Huang, W. Jiang, L. Duan, *J. Mater. Chem. C* **2018**, *6*, 5577.
- [16] K. Phlipps, *Investigation in Linker Functionality of Main-Chain Thermally Activated Delayed Fluorescence Polymers and Through-Space Charge Transfer in Supramolecular Polymers*, **2021**.
- [17] Y. Yang, S. Wang, Y. Zhu, Y. Wang, H. Zhan, Y. Cheng, *Adv. Funct. Mater.* **2018**, *28*, 1706916.
- [18] X. Ban, A. Zhu, T. Zhang, Z. Tong, W. Jiang, Y. Sun, *Chem. Commun.* **2017**, *53*, 11834.
- [19] X. Yin, Y. He, X. Wang, Z. Wu, E. Pang, J. Xu, J. Wang, *Front. Chem.* **2020**, *8*, 725.
- [20] Y. J. Cho, K. S. Yook, J. Y. Lee, *Adv. Mater.* **2014**, *26*, 6642.
- [21] Y. J. Kang, J. Y. Lee, *Dye. Pigm.* **2017**, *138*, 176.
- [22] F. M. Xie, Z. D. An, M. Xie, Y. Q. Li, G. H. Zhang, S. J. Zou, L. Chen, J. De Chen, T. Cheng, J. X. Tang, *J. Mater. Chem. C* **2020**, *8*, 5769.
- [23] C. Shi, D. Liu, J. Li, Z. He, K. Song, B. Liu, Q. Wu, M. Xu, *Dye. Pigm.* **2022**, *204*, 110430.
- [24] O. Sachnik, X. Tan, D. Dou, C. Haese, N. Kinaret, K.-H. Lin, D. Andrienko, M. Baumgarten, R. Graf, G.-J. A. H. Wetzelaer, J. J. Michels, P. W. M. Blom, *Nat. Mater.* **2024**, *12*, 2302000.
- [25] A. Bucinskas, K. Ivaniuk, G. Baryshnikov, O. Bezikonnyi, P. Stakhira, D. Volyniuk, B. Minaev, H. Ågren, Y. Zhydachevskyy, J. V. Grazulevicius, *Org. Electron.* **2020**, *86*, 105894.
- [26] G. Jiang, F. Li, X. Kong, J. Fan, Y. Song, C. K. Wang, L. Lin, *J. Lumin.* **2020**, *219*, 116899.
- [27] I. Hladka, D. Volyniuk, O. Bezikonnyi, V. Kinzhybalo, T. J. Bednarchuk, Y. Danyliv, R. Lytvyn, A. Lazauskas, J. V. Grazulevicius, *J. Mater. Chem. C* **2018**, *6*, 13179.
- [28] A. Maggiore, Y. Qu, R. Guillot, P. Pander, M. Vasylieva, P. Data, F. B. Dias, P. Audebert, G. Clavier, F. Miomandre, *J. Phys. Chem. B* **2022**, *126*, 2740.
- [29] S. M. Bonesi, R. Erra-Balsells, *J. Lumin.* **2001**, *93*, 51.
- [30] J. R. Cha, C. W. Lee, J. Y. Lee, M. S. Gong, *Dyes Pigm.* **2016**, *134*, 562.
- [31] H. L. Lee, K. H. Lee, J. Y. Lee, *Adv. Opt. Mater.* **2020**, *8*, 2001025.
- [32] K. Thakur, B. van der Zee, G. J. A. H. Wetzelaer, C. Ramanan, P. W. M. Blom, *Adv. Opt. Mater.* **2022**, *10*, 2101784.
- [33] T.-L. Wu, M.-J. Huang, C.-C. Lin, P.-Y. Huang, T.-Y. Chou, R.-W. Chen-Cheng, H.-W. Lin, R.-S. Liu, C.-H. Cheng, *Nat. Photon.* **2018**, *12*, 235.
- [34] S. Sem, S. Jenatsch, K. Stavrou, A. Danos, A. P. Monkman, B. Ruhstaller, *J. Mater. Chem. C* **2022**, *10*, 4878.
- [35] G. H. Kim, R. Lampande, J. B. Im, J. M. Lee, J. Y. Lee, J. H. Kwon, *Mater. Horizons* **2017**, *4*, 619.
- [36] T. Matulaitis, P. Imbrasas, N. A. Kukhta, P. Baronas, T. Bučiūnas, D. Banevičius, K. Kazlauskas, J. V. Gražulevičius, S. Juršėnas, *J. Phys. Chem. C* **2017**, *121*, 23618.
- [37] A. J. Horsewill, I. B. I. Tomsah, *Solid State Nucl. Magn. Reson.* **1993**, *2*, 61.
- [38] K. Saalwächter, I. Schnell, *Solid State Nucl. Magn. Reson.* **2002**, *22*, 154.
- [39] M. R. Hansen, R. Graf, H. W. Spiess, *Chem. Rev.* **2016**, *116*, 1272.
- [40] J. Eng, T. J. Penfold, *Chem. Rec.* **2020**, *20*, 831.
- [41] A. Wada, Q. Zhang, T. Yasuda, I. Takasu, S. Enomoto, C. Adachi, *Chem. Commun.* **2012**, *48*, 5340.
- [42] E. E. Bas, P. Ulukan, A. Monari, V. Aviyente, S. Catak, *J. Phys. Chem. A* **2022**, *126*, 473.
- [43] H. S. Kim, S.-R. Park, M. C. Suh, *J. Phys. Chem. C*, **2017**, *121*, 13986.
- [44] K. Shizu, M. Uejima, H. Nomura, T. Sato, K. Tanaka, H. Kaji, C. Adachi, *Phys. Rev. Appl.* **2015**, *3*, 014001.
- [45] J. S. Ward, R. S. Nobuyasu, A. S. Batsanov, P. Data, A. P. Monkman, F. B. Dias, M. R. Bryce, *Chem. Commun.* **2016**, *52*, 2612.
- [46] K. Wang, C. J. Zheng, W. Liu, K. Liang, Y. Z. Shi, S. L. Tao, C. S. Lee, X. M. Ou, X. H. Zhang, *Adv. Mater.* **2017**, *29*, 1.
- [47] T. Serevičius, R. Skaisgiris, J. Dodonova, K. Kazlauskas, S. Juršėnas, S. Tumkevičius, *Phys. Chem. Chem. Phys.* **2019**, *22*, 265.